

<https://doi.org/10.1038/s41612-024-00645-x>

Unraveling the Indian monsoon's role in fueling the unprecedented 2022 Marine Heatwave in the Western North Pacific

Check for updates

Qianghua Song^{1,2,3}, Chunzai Wang^{1,3}✉, Yulong Yao^{1,3}✉ & Hanjie Fan⁴

An unprecedented marine heatwave (MHW) event occurred in the middle-high latitudes of the western North Pacific during the summer of 2022. We demonstrate that excessive precipitation thousands of kilometers away fuels this extreme MHW event in July 2022. In the upper atmosphere, a persistent atmospheric blocking system, forming over the MHW region, reduces cloud cover and increases shortwave radiation at the ocean surface, leading to high sea surface temperatures. Atmospheric perturbations induced by latent heat release from the extreme precipitation in the Indian summer monsoon region enhance this atmospheric blocking through the propagation of quasi-stationary Rossby waves. Our hypothesis is verified by using a numerical model that is forced with the observed atmospheric anomalous diabatic heating. This study sheds light on how a subtropical extreme event can fuel another extreme event at middle-high latitudes through an atmospheric teleconnection.

During July 2022, a record-breaking marine heatwave (MHW) occurred in the middle-high latitudes of the western North Pacific, specifically in the Okhotsk Sea and the Western Bering Sea (referred to as OSWBS)¹. For example, sea surface temperature (SST) anomalies in the OSWBS region can be as high as 5 °C, with the category of MHW reaching a severity of Extreme (Fig. 1 and Supplementary Fig. 1). Previous studies have focused more on the physical mechanisms of middle-high latitudes MHWs in the Northeast Pacific, such as “the Blob 1.0” and “the Blob 2.0”, and the results suggest that atmospheric forcing plays a crucial role in these events^{2–7}. However, little attention has been paid to MHWs in the middle-high latitudes of the western North Pacific, and its underlying physical mechanisms have not been elucidated.

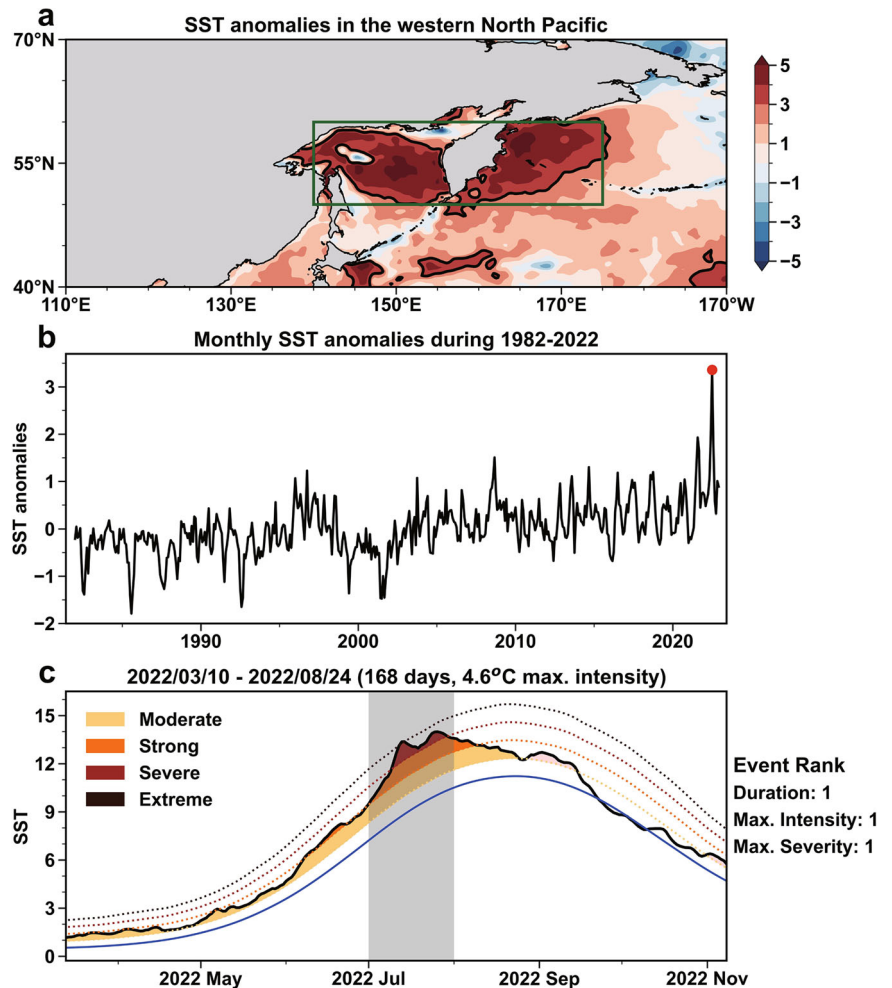
Most studies have shown that the occurrence of MHWs is typically associated with atmospheric forcings and oceanic dynamics^{8–10}. In addition, climate variability, such as the El Niño–Southern Oscillation (ENSO) and the Indian Ocean Dipole (IOD), can also contribute to MHWs^{4,11,12}. Atmospheric forcings, which usually manifest as atmospheric blocking high-pressure systems, can reduce cloud cover and thus increase the amount of shortwave radiation received by the oceans^{9,13}. Furthermore, they also suppress surface winds and decrease latent heat loss¹⁴. The MHW occurred in the OSWBS in July 2022 is also driven by atmospheric blocking high-pressure system. Interestingly, the intensity of this atmospheric blocking high-pressure system, according to our

research, is associated with subtropical precipitation in the Indian summer monsoon region. A similar process was observed during the severe droughts in South America and MHWs in the South Atlantic in 2013–2014¹⁵. Tropical deep convection over the Indian Ocean associated with the Madden-Julian Oscillation triggered the propagation of the Rossby waves across the South Pacific to the tip of South America, resulting in strong atmospheric blocking over South America and the South Atlantic.

In the summer of 2022, southern Pakistan, which belongs to the region of the Indian summer monsoon, experienced record-breaking monsoon rainfall. There is a clear link between this extreme precipitation and heatwaves in China's Yangtze River basin through a stationary Rossby wave-like pattern^{15,16}. However, the subsequent impacts triggered by this extreme rainfall event are not fully understood, especially its potential impacts on MHWs at middle-high latitudes. Additionally, summer rainfall over southern Pakistan has increased since 2000 due to spring warming in the Middle East¹⁷. In this study, we explore the physical processes by which extreme Indian summer monsoon precipitation fueled the unprecedented MHW in the middle-high latitudes OSWBS region in July 2022. Our findings elucidate the mechanism by which a subtropical extreme event can fuel a subsequent extreme event at middle-high latitudes through an atmospheric teleconnection, thereby enhancing the predictive capability for MHWs in the OSWBS region.

¹State Key Laboratory of Tropical Oceanography, South China Sea Institute of Oceanology, Chinese Academy of Sciences, Guangzhou, China. ²Global Ocean and Climate Research Center, South China Sea Institute of Oceanology, Chinese Academy of Sciences, Guangzhou, China. ³University of Chinese Academy of Sciences, Beijing, China. ⁴School of Atmospheric Sciences, Sun Yat-sen University, Zhuhai, China. ✉e-mail: cwang@scsio.ac.cn; ylyao@scsio.ac.cn

Fig. 1 | The MHW characteristics in the western North Pacific in 2022. a SST anomalies (units: °C) in the western North Pacific in July 2022. The area surrounded by the black contour lines indicates SST anomalies exceeding 3 °C, and the green box represents the study area in this paper (referred to as the OSWBS region, 50°N–60°N, 140°E–175°E). **b** Time series of monthly mean SST anomalies (units: °C) in the green box above for the period 1982–2022. The red dot marks July 2022. **c** The evolution of MHWs in the OSWBS region during 2022. The thick solid black curve indicates the area-averaged SST (units: °C) time series in 2022 and the solid blue curve is the smoothed climatological mean SST in the OSWBS region. The yellow, orange, red and dark red dotted curves denote the levels for Moderate, Strong, Severe, and Extreme categorization, respectively (see Methods). The MHW events during the period are color-shaded based on their respective categories, with pink shading indicating MHWs other than the highlighted event in each panel. The gray shading represents July 2022, with SST reaching the highest values. The duration, maximum intensity, and maximum severity of the 2022 MHW event were all ranked first in the history of OSWBS MHWs that have occurred.



Results

Characteristics of the unprecedented MHW

An unprecedented MHW event of high-intensity and long-duration occurred in the western North Pacific OSWBS region during the summer of 2022. The MHW peaked in July and the SST anomalies reached up to 5 °C in some areas of the OSWBS (Fig. 1a). In addition, there were over 1.5 million square kilometers of ocean with SST anomalies above 3 °C. Such large areas of warm sea water have placed SST anomaly of OSWBS in July 2022 at the top in history (Fig. 1b) and could have a severe impact on the marine ecosystems in this region. The MHW event in the OSWBS in 2022 lasted 168 days and reached Extreme level with a maximum intensity of 4.6 °C (Fig. 1c). As a result, the number of total days and the maximum intensity of MHWs in the OSWBS in 2022 are at their highest levels ever.

We also confirmed an extreme MHW in the OSWBS in July 2022 using other sets of satellite and reanalysis data (see Methods) (Supplementary Fig. 1a, c). During this event, the regional mean SST anomalies exceeded 3 °C, which was the highest in the historical record (Supplementary Fig. 1b, d).

Atmospheric forcing on MHW

Given that extratropical blocking highs have large spatial scales and can persist for weeks to months, they have the potential to significantly increase ocean temperatures over a large geographic region for a considerable period of time. Therefore, the occurrence of middle-high latitudes MHWs is often associated with atmospheric forcing processes⁹. To explore the role played by atmospheric forcing during the MHW, it is essential to assess atmospheric conditions over the western North Pacific in July 2022. Observational data show that there are atmospheric blocking high-pressure systems

in both the upper-level (200 hPa) and mid-level (500 hPa) troposphere over the OSWBS region (Supplementary Fig. 2). The barotropic structure indicates that the atmospheric blocking system may be a teleconnection pattern triggered by other perturbations^{18–20}. Therefore, we also calculated the Rossby wave activity flux at 200 hPa in the Northern Hemisphere in July 2022. Obviously, there is a train of stationary Rossby waves originating from central Asia (Fig. 2a). When the wave energy reaches the Mongolian Plateau, it splits into two branches. The southern branch propagates southward to form a high-pressure system over the Bohai Sea, which, combined with the high-pressure system over Central Asia, constitutes part of the circumglobal teleconnection^{21–23} (Supplementary Fig. 2). The northern branch converges in the OSWBS region to form a powerful blocking high-pressure system.

Once the blocking system forms, it suppresses convection and causes strong subsidence, leading to reduced cloud cover and increased solar radiation. Figure 2b, c show the cloud fraction anomalies and surface shortwave radiation anomalies in the western North Pacific in July 2022, respectively. A significant decrease in cloud fraction and a large increase in shortwave radiation are observed in the OSWBS region. In contrast to the increase in shortwave radiation, the changes in the other heat fluxes (longwave radiation, sensible heat flux, and latent heat flux) are relatively small (Supplementary Figs. 3, 4). Notably, areas with less cloud cover and higher shortwave radiation coincide with regions of warmer SST anomalies, suggesting that the reduction in cloud cover leads to an increase in shortwave radiation, resulting in an increase in the mixed layer temperature. The cloud fraction in the OSWBS region reached the second lowest on record in July 2022, which led to record high values of shortwave radiation during the same period, as there was a strong negative correlation between them ($r = -0.877$, $p < 0.01$; Fig. 2d).

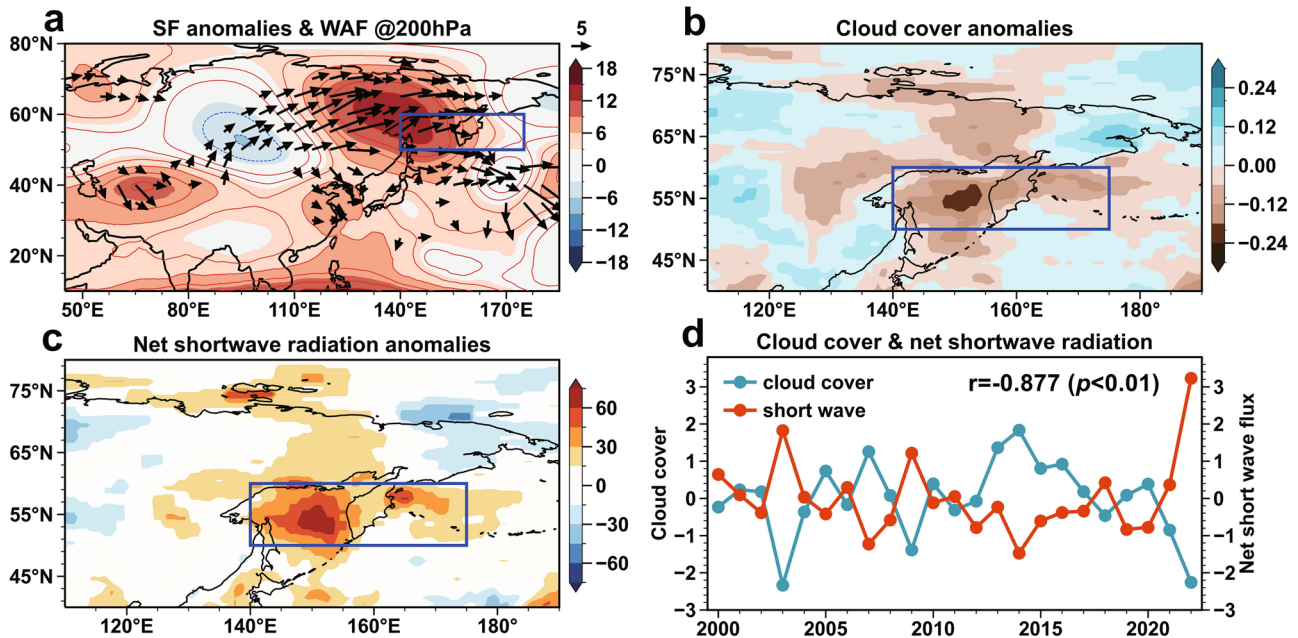


Fig. 2 | Atmospheric conditions in the western North Pacific in July 2022.
 a Stream function anomalies (SF, shading and contour, units: $10^6 \text{ m}^2 \text{ s}^{-1}$) and wave activity flux (WAF, black vectors, values smaller than 3 are filtered out, units: $\text{m}^2 \text{ s}^{-2}$) at 200 hPa. Anomalies of (b) cloud cover (units: 1) and (c) surface net shortwave

radiation (units: $\text{J s}^{-1} \text{ m}^{-2}$) in July 2022, along with (d) inter-annual variation in the standardized cloud cover and shortwave radiation for the OSWBS (blue box) regional average in July from 2000 to 2022 ($r = -0.877, p < 0.01$), where the red curve represents shortwave radiation and the blue curve represents cloud cover.

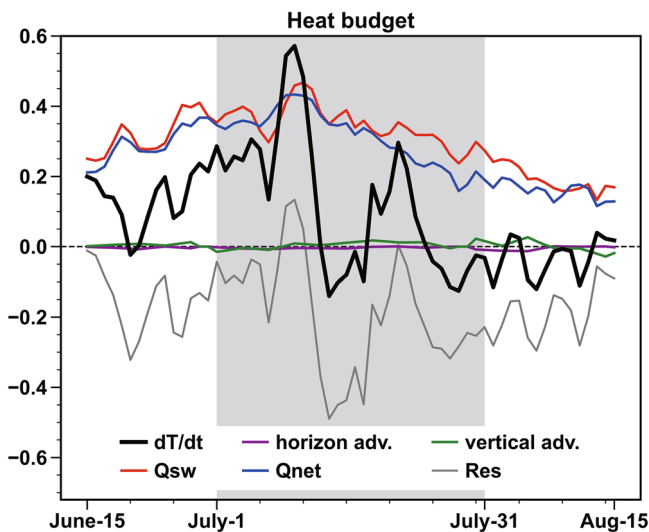


Fig. 3 | The ocean mixed layer heat budget in the OSWBS region. The daily evolution of the heat budget (units: $^{\circ}\text{C day}^{-1}$) in the OSWBS region from mid-June to mid-August 2022 using daily OISST and ECCO2 data. Shading represents July. The black curve represents the tendency of SST; the blue curve represents the total surface net heat flux; the red curve represents the surface net shortwave radiation; the purple (green) curve represents horizontal (vertical) advection; the gray curve denotes the residual term. The correlation coefficient between surface net shortwave radiation and the rate of temperature change is 0.66 ($p < 0.01$) in July.

To further verify whether the SST warming is primarily caused by surface heat fluxes, we calculated the daily mixed layer heat budget in the OSWBS region (Fig. 3). The results show that the SST tendency depends on the surface heat fluxes received by the ocean, with the most dominant component being the enhanced surface shortwave radiation. The contribution of oceanic heat advection to the SST tendency is negligible. Thus, the main cause of ocean warming is a positive anomaly in the net shortwave radiation ($r = 0.66, p < 0.01$).

The role of Indian summer monsoon’s rainfall

The above analysis indicates that the atmospheric blocking high-pressure system is the major factor influencing the variability of MHWs in the OSWBS, so it is vital to investigate what triggers such anomalous atmospheric blocking. According to the analysis of the stationary Rossby waves (Fig. 2a), the wave activity flux originates from a high-pressure system over Central Asia. Previous studies have indicated that this high-pressure system is commonly associated with the circumpolar teleconnection and is often prompted by Indian summer monsoon rainfall^{22–24}. In July 2022, an unusually extreme rainfall event occurred in the Indian summer monsoon region ($15^{\circ}\text{N}–35^{\circ}\text{N}, 60^{\circ}\text{E}–80^{\circ}\text{E}$), particularly in southern Pakistan (Fig. 4a). The amount of precipitation in July 2022 ranked first compared to historical records and greatly exceeded the average (Fig. 4b; WMO¹). During the extreme precipitation, the condensation of water vapor release large amounts of latent heat, which increases diabatic heating and induces atmospheric perturbations^{25–27}. We define the regional average vertical integral of divergence of latent heat flux in the region $15^{\circ}\text{N}–35^{\circ}\text{N}, 60^{\circ}\text{E}–80^{\circ}\text{E}$ as the latent heat release index (see Methods). Similarly, the record-breaking latent heat release index is simultaneously detected during this extreme precipitation event, and there is a significant positive correlation between precipitation and latent heat release index ($r = 0.898, p < 0.01$; Fig. 4b).

We perform a regression analysis of geopotential height and wind on the latent heat release index in July from 1979 to 2022. Figure 5 shows that the regressed geopotential height and wind are very similar to the July 2022 observations. The positive geopotential height anomalies appeared in central Asia, the Bohai Sea, and the OSWBS region. Especially, the positive geopotential height anomalies in the OSWBS region are very strong, accompanied by strong anticyclonic circulation, forming a powerful blocking system. Therefore, we hypothesize that the atmospheric circulation pattern across the Northern Hemisphere, especially in the OSWBS region, is primarily driven by diabatic heating from latent heat released by extreme precipitation in southern Pakistan.

Numerical model experiments

To prove our hypothesis, we conduct diabatic heating-forcing model experiments using the Community Atmospheric Model version 5 (CAM5;

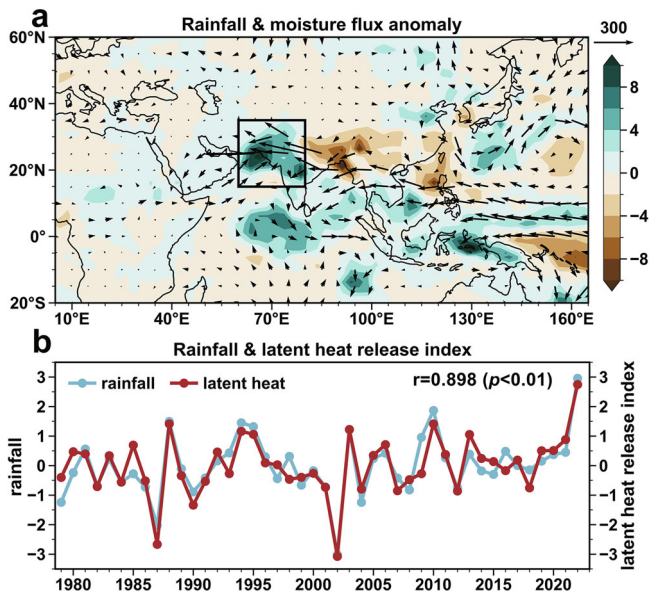


Fig. 4 | The extreme precipitation and latent heat release in the Indian summer monsoon region in July 2022. a Anomalies of precipitation (shading, units: mm day⁻¹) and vertically integrated moisture flux from 1000 hPa to 100 hPa (vectors, units: kg m⁻¹ s⁻¹) in July 2022, with the black box indicating the region of Indian summer monsoon (15°N–35°N, 60°E–80°E). **b** Inter-annual variation in the standardized regional average rainfall (blue curve) and the standardized latent heat release index (red curve) in the black box region in July ($r=0.898$, $p<0.01$), where the regional average vertical integral of divergence of latent heat flux is defined as the latent heat release index (see Methods).

see Methods). According to the observed data (Supplementary Fig. 5), the regional average vertically integrated diabatic heating ($18 \text{ J s}^{-1} \text{ m}^{-2}$) in July 2022 in the extreme precipitation area of southern Pakistan (17°N – 30°N , 60°E – 73°E) is approximately three times that of the mean state ($6 \text{ J s}^{-1} \text{ m}^{-2}$) in July. Therefore, we tripled the diabatic heating rate in July at the corresponding location (17°N – 30°N , 60°E – 73°E) in the CAM5 model (Fig. 6a). Figure 6b shows the variations in the vertical heating profiles for the heating-forcing experiment (HEATING_run) and the control experiment (CTL_run) as well as the difference between them. The maximum diabatic heating rate appears at altitudes of about 500–600 hPa. As expected, the introduction of a three times diabatic heating rate in July in southern Pakistan is followed by a rapid response of the atmospheric circulation, generating patterns similar to the observations in July 2022 (Fig. 6c). A high-pressure anticyclone appears in central Asia and a low-pressure system appears in Mongolia. The atmospheric circulation in the OSWBS region exhibits an extraordinary blocking high-pressure system. Consequently, the numerical model confirms that the atmospheric blocking high pressure over the OSWBS region, which is responsible for the unprecedented MHW, is triggered by the latent heat of extreme precipitation in southern Pakistan.

Discussion

In this study, we investigate how Indian summer monsoon’s excessive precipitation fuels the middle-high latitudes MHW by exploring the physical mechanism of the extreme MHW in the OSWBS region in July 2022. The unprecedented MHW event breaks historical record in terms of intensity, with the maximum SST anomalies can be as high as 5 °C. Through the analysis of the ocean mixed layer heat budget, we reveal that the primary factor causing the SST rise is the atmospheric forcing. A strong atmospheric blocking high-pressure system persists in the upper atmosphere over the OSWBS region. This blocking high-pressure system suppresses convection and reduces cloud cover, which increases shortwave radiation received by the ocean, leading to a rapid rise in SST. The atmospheric blocking system is generated through atmospheric teleconnection. Specifically, latent heat

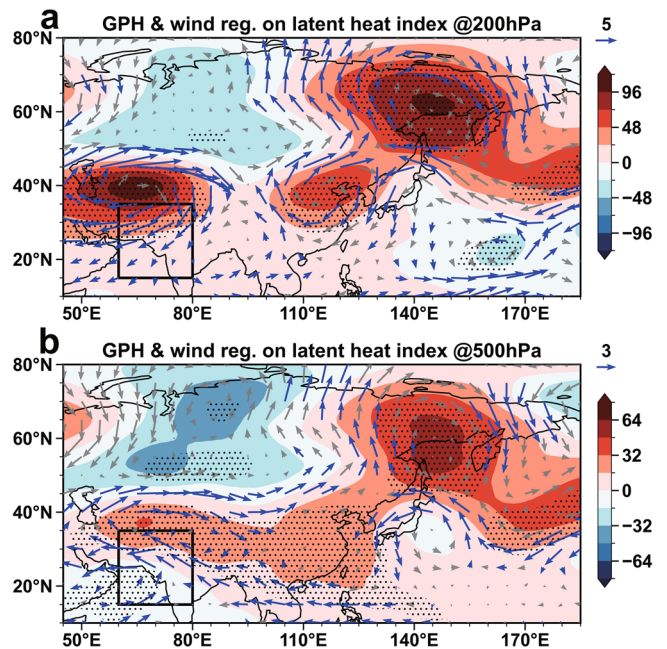


Fig. 5 | Impact of the extreme precipitation on atmospheric circulation. Regression of (a) 200 hPa and (b) 500 hPa geopotential height (GPH, shading, units: gpm) and wind (vectors, units: m s⁻¹) on the latent heat release index in July from 1979 to 2022. Dotted areas and blue vectors represent statistical significance at the 90% confidence level. Black box indicates the region of Indian summer monsoon (15°N–35°N, 60°E–80°E), which is also the region where the latent heat release index is defined.

released from the extreme precipitation in the Indian summer monsoon region triggers quasi-stationary Rossby waves to propagate into the OSWBS region, leading to energy accumulation and the formation of a stable atmospheric blocking high-pressure system (Fig. 7). By employing the CAM5 numerical model, we substantiate our hypothesis that heightened diabatic heating in southern Pakistan experiencing extreme precipitation induces a robust atmospheric blocking high-pressure system over OSWBS regions.

Through a case study of an extreme MHW event in July 2022, we have successfully established a physical link between the Indian summer monsoon rainfall and MHWs in the OSWBS. This raises the question of whether the relationship between Indian summer monsoon precipitation and OSWBS SST is generally applicable. To answer this question, we calculate the correlation coefficient between these two variables in July from 1982 to 2022 (Supplementary Fig. 6). From 1982 to 2010, there is no correlation between the precipitation and the SST. However, a strong correlation ($r=0.97$, $p<0.01$) is observed after 2011. The reasons for this shift deserve further exploration, and it is also important to note that Indian summer monsoon precipitation can improve the predictive ability of OSWBS MHW.

It should not be overlooked that the residual term in the heat budget is also important in this study. The residual term represents unresolved processes, such as vertical turbulent diffusion or observational errors¹³. The residual term comes mainly from observational errors, and the substantial residual term from data assimilation or across long-term average fields has been noticeable in many previous studies^{2,3,6,28,29}. Despite these concerns, we believe it is credible to conclude that atmospheric blocking fuels MHW due to the dominant role of shortwave radiation in SST increase.

The extreme rainfall in the Indian summer monsoon region regulated by the Indian Ocean played a dominant role in the extreme MHW event in the western North Pacific. This suggests that inter-basin interactions are a non-negligible mechanisms influencing the intensity and duration of MHWs. Previous studies have demonstrated that inter-basin interactions have an important influence on the occurrence and development of MHWs, such as the Southwest Atlantic MHW in 2013–2014, the North Pacific MHWs in 2013–2015 and 2018–2022, and the western North Pacific

Fig. 6 | The forcings and results of the CAM5 model. **a** Spatial distribution of differences between HEATING_run and CTL_run in the diabatic heating rates (units: $J s^{-1} kg^{-1}$) at 500 hPa. **b** Vertical profiles of the regional average diabatic heating rates (units: $J s^{-1} kg^{-1}$) of HEATING_run (red curve), CTL_run (blue curve) and the difference between them (orange curve) in the region of 17°N–30°N, 60°E–73°E. **c** Composite differences in geopotential height (GPH, shading, units: gpm) and wind (vectors, units: $m s^{-1}$) at 200 hPa between the HEATING_run and CTL_run.

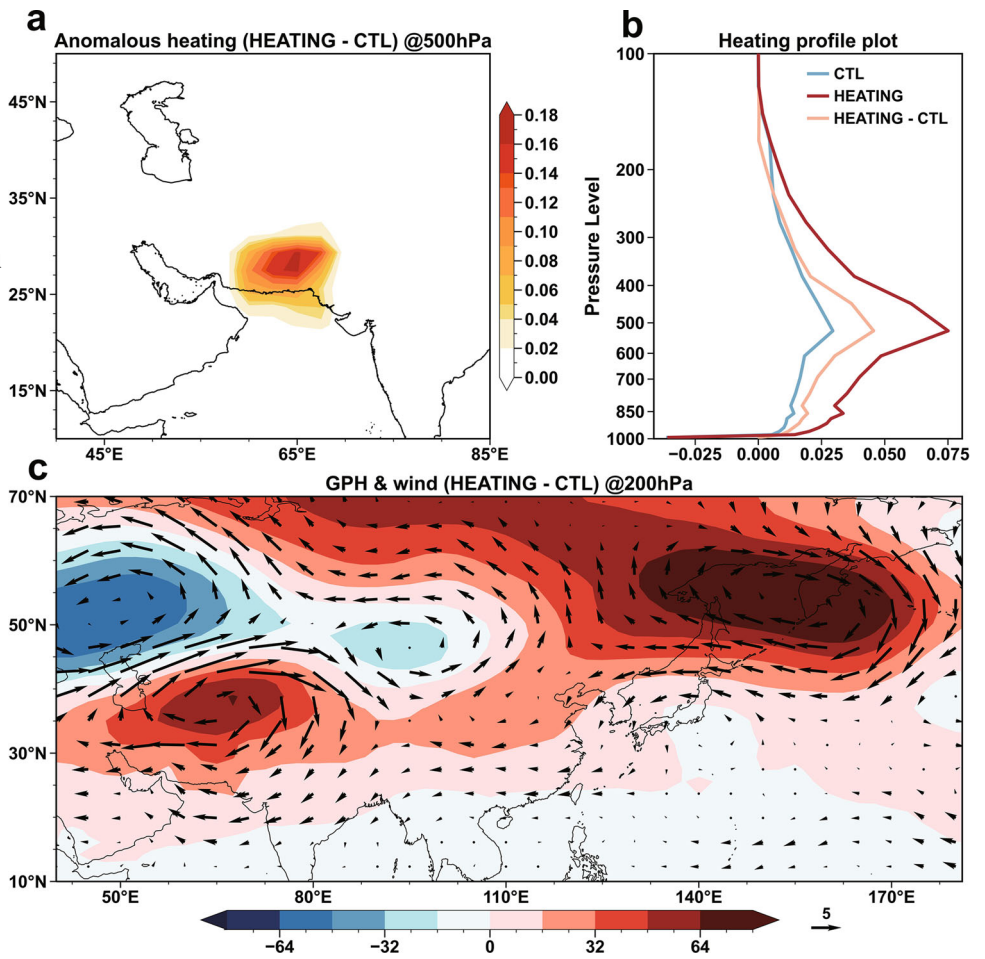
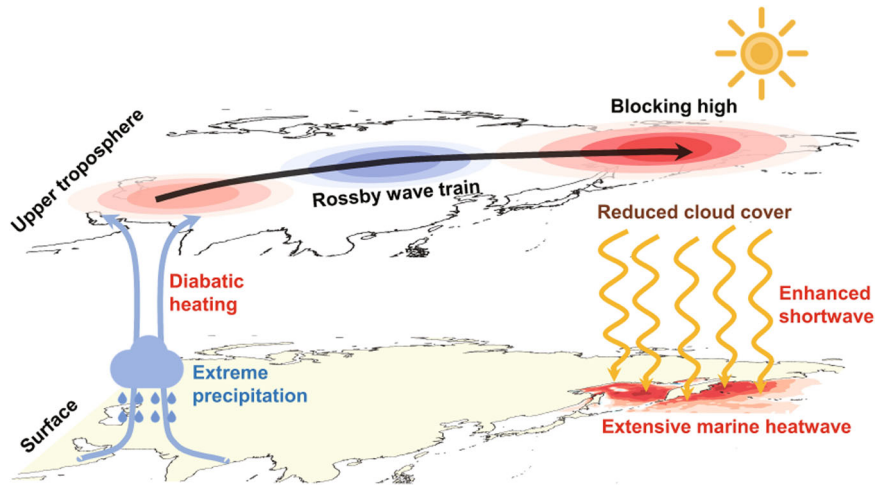


Fig. 7 | Schematic representation of the forcing mechanism of the OSWBS MHW in July 2022. The extreme precipitation releases a significant amount of diabatic heating in southern Pakistan, which triggers a Rossby wave train that forms a blocking high-pressure system over the OSWBS region. The blocking system suppresses convection, reduces cloud cover, and increases the shortwave radiation received by the ocean. With the ocean receiving a large influx of shortwave radiation, the SST rapidly increases, resulting in the extreme MHW in the OSWBS region.



MHWs in summer 2020^{5,13,30,31}. Therefore, more attention should be given to the role of inter-basin interactions when studying the mechanisms of MHWs, especially those occurring at middle-high latitudes³².

Methods

Data sources

The daily SST data used in this study are from the National Oceanic and Atmospheric Administration (NOAA) Optimum Interpolation (OI) SST dataset version 2.1 (OISST v2.1)³³, with a resolution of $0.25^\circ \times 0.25^\circ$,

covering the period from 1982 to 2022. Additionally, to validate the accuracy of the OISST data, we also utilized the European Space Agency (ESA) SST dataset³⁴ and the fifth generation of the European Center for Medium-Range Weather Forecasts atmospheric reanalysis dataset (ERA5) SST dataset³⁵. Both of the two daily SST datasets cover the period from 1982 to 2022 and have been uniformly interpolated to a resolution of $0.25^\circ \times 0.25^\circ$.

The monthly atmospheric data consist of the ERA5 dataset³⁵ at a resolution of $1^\circ \times 1^\circ$, spanning from 1979 to 2022. The ERA5 atmospheric variables include geopotential, wind speed, air temperature, specific

humidity, mean surface net latent and sensible heat flux. The monthly precipitation data are obtained from the Global Precipitation Climatology Project (GPCP) Monthly Analysis Product³⁶, covering the period from 1979 to 2022, with a spatial resolution of 2.5° × 2.5°.

Moreover, to calculate the ocean mixed layer heat budget in the study area, Estimating the Circulation and Climate of the Ocean Phase II (ECCO2) daily dataset³⁷ from the Jet Propulsion Laboratory of National Aeronautics and Space Administration (NASA/JPL) at a resolution of 0.25° × 0.25° is employed, spanning from 1992 to 2022, including surface net shortwave radiation, surface net heat flux, mixed layer depth, potential temperature, horizontal and vertical velocity.

We also utilize satellite-derived data in this study. The surface net shortwave radiation, surface net longwave radiation, and cloud cover used in the research are all from the Clouds and the Earth's Radiant Energy System (CERES) satellite-derived monthly dataset³⁸, which is currently available on a 1° × 1° grid from March 2000 to June 2023.

Definition and categorization of MHWs

We adopt the Hobday et al.³⁹ definition method to identify MHW events. A MHW event is defined as SST being warmer than the 90th percentile based on a baseline climatology for at least five consecutive days and two successive events with a break of 2 days or less between are considered a single continuous event. The seasonally varying climatology and 90th percentile threshold is calculated for each day of the year using daily temperature values across all years and within an 11-day window centered on the day, and are then smoothed using a 31-day moving window. The period used to define the climatology and 90th percentile threshold is 1982–2022.

The categorization of MHWs is derived from the work of Hobday et al.⁴⁰ and Kajtar et al.⁴¹. A specific MHW category can be established by considering a multiple of the local difference between the fixed climatological mean and the 90th percentile of the climatological distribution. Specifically, the formula for calculating severity is as follows:

$$\text{Severity} = \frac{\text{SSTA}}{\text{Threshold} - \text{Climatology}} \quad (1)$$

Using the multiple of difference, severity can be assigned to each point in time and space during an MHW event. These severity categories are classified as Moderate (1–2×), Strong (2–3×), Severe (3–4×), and Extreme (> 4×).

Wave activity flux

In order to better diagnose the horizontal propagation characteristics of Rossby waves in the atmosphere in July 2022, the T-N wave activity flux (WAF) developed by Takaya and Nakamura⁴² is also calculated in this study. The formula is as follows:

$$\vec{W}_h = \frac{p \cos \varphi}{2 |\vec{U}_c|} \left(\begin{array}{l} \frac{u_c}{a^2 \cos^2 \varphi} \left[\left(\frac{\partial \psi'}{\partial \lambda} \right)^2 - \psi' \frac{\partial^2 \psi'}{\partial \lambda^2} \right] + \frac{v_c}{a^2 \cos \varphi} \left[\frac{\partial \psi'}{\partial \lambda} \frac{\partial \psi'}{\partial \varphi} - \psi' \frac{\partial^2 \psi'}{\partial \lambda \partial \varphi} \right] \\ \frac{u_c}{a^2 \cos \varphi} \left[\frac{\partial \psi'}{\partial \lambda} \frac{\partial \psi'}{\partial \varphi} - \psi' \frac{\partial^2 \psi'}{\partial \lambda \partial \varphi} \right] + \frac{v_c}{a^2} \left[\left(\frac{\partial \psi'}{\partial \varphi} \right)^2 - \psi' \frac{\partial^2 \psi'}{\partial \varphi^2} \right] \end{array} \right) \quad (2)$$

where \vec{W}_h is the horizontal T-N wave activity flux vector; the φ and λ represent latitude and longitude, respectively; the variable $\vec{U}_c = (u_c, v_c)$ represents the climatological mean horizontal wind vector; u_c and v_c are the climatological mean zonal and meridional winds, respectively; ψ' represents the perturbation stream-function; a is Earth's radius (6.37×10^6 m), and $p = (\text{pressure}/1000 \text{ hPa})$. The climatological mean and perturbation were calculated based on the period of 1979–2022.

Ocean mixed layer heat budget

We utilize daily OISST and ECCO2 data to calculate the mixed layer heat budget in the OSWBS region. The equation for the mixed layer heat budget

can be expressed as follows⁴³:

$$\frac{\partial T}{\partial t} = -(\vec{V} \cdot \nabla T) + \frac{Q_{net}}{\rho_0 C_p H} + \text{Residual} \quad (3)$$

In the equation, T represents the mixed layer temperature; \vec{V} signifies horizontal and vertical velocity, and ∇ represents the gradient operator; Q_{net} denotes the surface net heat flux (the sum of shortwave radiation, longwave radiation, latent heat flux, and sensible heat flux) into the ocean; ρ_0 and C_p represent the sea water density (1025 kg m^{-3}) and specific heat capacity ($3996 \text{ J kg}^{-1} \text{ K}^{-1}$), respectively; H is the mixed layer depth, which is taking the regional average mixed layer depth of OSWBS. Due to the uniformity of temperature in the mixed layer, here we use the SST from OISST dataset instead of the mixed layer temperature. Other variables, including surface net heat flux, surface net shortwave radiation, potential temperature, mixed layer depth, horizontal and vertical velocity, are sourced from the ECCO2 dataset.

Latent heat release index

The latent heat release index is defined as the regional average vertical integral of divergence of latent heat flux in the area of Indian summer monsoon (black box in Fig. 4a, 15°N–35°N, 60°E–80°E). The divergence of latent heat flux in the atmosphere is calculated as follows⁴⁴:

$$\nabla(\vec{E}_1) = \nabla \left\{ \vec{V} q \left[L_v + (C_{pv} - C_w) T \right] \right\} \quad (4)$$

where ∇ represents the gradient operator; \vec{E}_1 is the latent heat flux; \vec{V} and q represent horizontal wind and specific humidity; g is the gravitational acceleration (9.8 m s^{-2}); L_v , with a value approximately equal to $2.5 \times 10^6 \text{ J kg}^{-1}$, is the latent heat of vaporization; C_{pv} and C_w represent the specific heat of water vapor at constant pressure ($1846.1 \text{ J kg}^{-1} \text{ K}^{-1}$) and the specific heat of liquid water at 273.15 K ($4218 \text{ J kg}^{-1} \text{ K}^{-1}$), respectively; T indicates the air temperature. $\langle \nabla(\vec{E}_1) \rangle = \frac{1}{g} \int_{1000 \text{ hPa}}^{100 \text{ hPa}} \nabla(\vec{E}_1) dp$ represents the vertically integrated divergence of latent heat flux and the vertical integral is from 1000 hPa to 100 hPa.

Atmospheric diabatic heating

In order to more reasonably design the amount of atmospheric diabatic heating modified in the model, we calculate the actual atmospheric diabatic heating based on observational data. The formula of atmospheric diabatic heating is proposed by Yanai⁴⁵ and as following:

$$Q_1 = C_p \frac{\partial T}{\partial t} - C_p (\omega \sigma - \vec{V} \cdot \nabla T) \quad (5)$$

$$\sigma = \left(\frac{RT}{C_p p} \right) - \left(\frac{\partial T}{\partial p} \right) \quad (6)$$

where C_p denotes the specific heat at constant pressure ($1004.7 \text{ J kg}^{-1} \text{ K}^{-1}$), T and t are the air temperature and the time, respectively. ω represents the vertical velocity. σ is the static stability, R represents the gas constant ($287 \text{ J kg}^{-1} \text{ K}^{-1}$), p is the pressure, \vec{V} denotes the horizontal wind vector, and ∇ represents the horizontal gradient operator. Here, $\langle Q_1 \rangle = \frac{1}{g} \int_{1000 \text{ hPa}}^{100 \text{ hPa}} Q_1 dp$ represents the vertically integrated total diabatic heating.

Atmospheric general circulation model experiments

To examine the impact of latent heat release from extreme precipitation in the Indian summer monsoon region on atmospheric circulation, the Community Atmospheric Model version 5 (CAM5) is employed in this study for conducting model experiments⁴⁶. This model has demonstrated excellent capability in accurately reproducing the mean climate state and has been extensively utilized in numerous relevant studies.

All the runs in this study are conducted using a FC5 component with a horizontal resolution of approximately 2.5° longitude × 1.9° latitude and 31

vertical levels. Two sets of numerical model experiments are performed. The first set is the control run (referred to as CTL_run), which is forced by the default climatological mean SST and sea ice, without any additional atmospheric anomalous diabatic heating. The second set is the sensitivity experiment called HEATING_run, which also uses the default climatological mean global SST and sea ice as forcings. Additionally, in the 17°N–30°N, 60°E–73°E region, three times the anomalous atmospheric diabatic heating is added in July, which is based on the ratio between observational diabatic heating ($18 \text{ J s}^{-1} \text{ m}^{-2}$) in July 2022 and the historical July average diabatic heating ($6 \text{ J s}^{-1} \text{ m}^{-2}$). Each numerical experiment simulates the climate conditions for 30 years with a seasonal cycle, and the last 10 years of each experiment are compared using ensemble mean.

Statistical information

In this study, the statistical significance of the linear regression coefficient and Pearson correlation coefficient between two autocorrelated time series are assessed via a two-tailed Student's t-test.

The climatological period for the data used in this paper is defaulted to the period of 1979–2022. However, due to the varying release times of some datasets, the climatology of these data may differ. The climatology for all SST datasets (OISST/ESA/ERA5) spans the years 1982–2022. The climate state of ECCO2 spans from 1992 to 2022. As for shortwave radiation, longwave radiation, and cloud cover, based on CERES satellite observational data, a uniform climatological period of 2000–2022 is chosen for consistency.

Data availability

All data used in this study are publicly available online. NOAA/OAR/ESRL PSD provided the OISST high-resolution dataset from their Web site at <https://downloads.psl.noaa.gov/Datasets/noaa.oisst.v2.highres/>. The ERA5 reanalysis SST dataset can be downloaded from <https://doi.org/10.24381/cds.adbb2d47>. ERA5 reanalysis atmospheric dataset are available from ECMWF at <https://doi.org/10.24381/cds.6860a573>. The ESA Satellite observations SST dataset can be obtained from <https://doi.org/10.48670/moi-00169>. GPCP precipitation dataset is publicly available at <https://psl.noaa.gov/data/gridded/data.gpcp.html>. CERES surface radiation and cloud cover data are publicly available at <https://ceres.larc.nasa.gov/data/>. The ECCO2 data can be downloaded from https://ecco.jpl.nasa.gov/drive/files/ECCO2/cube92_latlon_quart_90S90N.

Code availability

The Python codes used to analyze the data and generate the main results presented in this study can be obtained from https://github.com/SongQiangH/OSWBS_MHW. The codes for MHW category in this study are publicly available at https://github.com/jbkajtar/mhw_australia.

Received: 21 December 2023; Accepted: 10 April 2024;

Published online: 16 April 2024

References

1. WMO. *State of the Climate in Asia 2022*. <https://wmo.int/resources/publications/state-of-climate-asia-2022> (2023).
2. Bond, N. A., Cronin, M. F. & Freeland, H. & Mantua, N. Causes and impacts of the 2014 warm anomaly in the NE Pacific. *Geophys. Res. Lett.* **42**, 3414–3420 (2015).
3. Amaya, D. J., Miller, A. J., Xie, S.-P. & Kosaka, Y. Physical drivers of the summer 2019 North Pacific marine heatwave. *Nat. Commun.* **11**, 1903 (2020).
4. Di Lorenzo, E. & Mantua, N. Multi-year persistence of the 2014/15 North Pacific marine heatwave. *Nat. Clim. Change* **6**, 1042–1047 (2016).
5. Zhao, Y. & Yu, J.-Y. Two Marine Heat Wave (MHW) Variants under a Basin-wide MHW Conditioning Mode in the North Pacific and Their Atlantic Associations. *J. Clim.* **36**, 8657–8674 (2023).
6. Chen, Z., Shi, J., Liu, Q., Chen, H. & Li, C. A Persistent and Intense Marine Heatwave in the Northeast Pacific During 2019–2020. *Geophys. Res. Lett.* **48**, e2021GL093239 (2021).

7. Xu, T., Newman, M., Capotondi, A. & Di Lorenzo, E. The Continuum of Northeast Pacific Marine Heatwaves and Their Relationship to the Tropical Pacific. *Geophys. Res. Lett.* **48**, 2020GL090661 (2021).
8. Oliver, E. C. J. et al. Marine Heatwaves. *Annu. Rev. Mar. Sci.* **13**, 313–342 (2021).
9. Holbrook, N. J. et al. Keeping pace with marine heatwaves. *Nat. Rev. Earth Environ.* **1**, 482–493 (2020).
10. Yao, Y. & Wang, C. Variations in Summer Marine Heatwaves in the South China Sea. *J. Geophys. Res. Oceans* **126**, e2021JC017792 (2021).
11. Liu, K., Xu, K., Zhu, C. & Liu, B. Diversity of Marine Heatwaves in the South China Sea Regulated by ENSO Phase. *J. Clim.* **35**, 877–893 (2022).
12. Zhang, Y., Du, Y., Feng, M. & Hu, S. Long-Lasting Marine Heatwaves Instigated by Ocean Planetary Waves in the Tropical Indian Ocean During 2015–2016 and 2019–2020. *Geophys. Res. Lett.* **48**, e2021GL095350 (2021).
13. Rodrigues, R. R., Taschetto, A. S., Sen Gupta, A. & Foltz, G. R. Common cause for severe droughts in South America and marine heatwaves in the South Atlantic. *Nat. Geosci.* **12**, 620–626 (2019).
14. Ge, Z.-A., Chen, L., Li, T. & Sun, M. Unraveling the formation mechanism of exceptionally strong marine heatwave in the Northeast Pacific in 2020. *J. Clim.* **36**, 8091–8111 (2023).
15. Wang, Z., Luo, H. & Yang, S. Different mechanisms for the extremely hot central-eastern China in July–August 2022 from a Eurasian large-scale circulation perspective. *Environ. Res. Lett.* **18**, 024023 (2023).
16. Tang, S. et al. Linkages of unprecedented 2022 Yangtze River Valley heatwaves to Pakistan flood and triple-dip La Niña. *npj Clim. Atmos. Sci.* **6**, 44 (2023).
17. Li, B. et al. Middle east warming in spring enhances summer rainfall over Pakistan. *Nat. Commun.* **14**, 7635 (2023).
18. Branstator, G. Horizontal Energy propagation in a Barotropic Atmosphere with Meridional and Zonal Structure. *J. Atmos. Sci.* **40**, 1689–1708 (1983).
19. Simmons, A. J., Wallace, J. M. & Branstator, G. W. Barotropic Wave Propagation and Instability, and Atmospheric Teleconnection. *Patterns J. Atmos. Sci.* **40**, 1363–1392 (1983).
20. Wirth, V., Riemer, M., Chang, E. K. M. & Martius, O. Rossby Wave Packets on the Midlatitude Waveguide—A Review. *Mon. Weather Rev.* **146**, 1965–2001 (2018).
21. Branstator, G. Circumglobal Teleconnections, the Jet Stream Waveguide, and the North Atlantic Oscillation. *J. Clim.* **15**, 1893–1910 (2002).
22. Ding, Q., Wang, B., Wallace, J. M. & Branstator, G. Tropical–Extratropical Teleconnections in Boreal Summer: Observed Interannual Variability. *J. Clim.* **24**, 1878–1896 (2011).
23. Ding, Q. & Wang, B. Circumglobal Teleconnection in the Northern Hemisphere Summer. *J. Clim.* **18**, 3483–3505 (2005).
24. Lin, H. Global Extratropical Response to Diabatic Heating Variability of the Asian Summer Monsoon. *J. Atmos. Sci.* **66**, 2697–2713 (2009).
25. Hagos, S. & Zhang, C. Diabatic heating, divergent circulation and moisture transport in the African monsoon system. *Quart. J. Roy. Meteor. Soc.* **136**, 411–425 (2010).
26. Nie, J., Dai, P. & Sobel, A. H. Dry and moist dynamics shape regional patterns of extreme precipitation sensitivity. *Proc. Natl Acad. Sci. USA* **117**, 8757–8763 (2020).
27. Jakob, C. & Schumacher, C. Precipitation and Latent Heating Characteristics of the Major Tropical Western Pacific Cloud Regimes. *J. Clim.* **21**, 4348–4364 (2008).
28. Cook, K. H., Vizy, E. K. & Sun, X. Multidecadal-scale adjustment of the ocean mixed layer heat budget in the tropics: examining ocean reanalyses. *Clim. Dyn.* **50**, 1513–1532 (2018).
29. Manta, G., Mello, S., Trinchin, R., Badagian, J. & Barreiro, M. The 2017 Record Marine Heatwave in the Southwestern Atlantic Shelf. *Geophys. Res. Lett.* **45**, 12,449–12,456 (2018).

30. Liang, Y.-C., Yu, J.-Y., Saltzman, E. S. & Wang, F. Linking the Tropical Northern Hemisphere Pattern to the Pacific Warm Blob and Atlantic Cold Blob. *J. Clim.* **30**, 9041–9057 (2017).
 31. Yao, Y., Wang, C. & Wang, C. Record-breaking 2020 summer marine heatwaves in the western North Pacific. *Deep Sea Res. Part II* **209**, 105288 (2023).
 32. Wang, C. Three-ocean interactions and climate variability: a review and perspective. *Clim. Dyn.* **53**, 5119–5136 (2019).
 33. Huang, B. et al. Improvements of the Daily Optimum Interpolation Sea Surface Temperature (DOISST) Version 2.1. *J. Clim.* **34**, 2923–2939 (2021).
 34. Lavergne, T. et al. Version 2 of the EUMETSAT OSI SAF and ESA CCI sea-ice concentration climate data records. *The Cryosphere* **13**, 49–78 (2019).
 35. Hersbach, H. et al. The ERA5 global reanalysis. *Quart. J. Roy. Meteor. Soc.* **146**, 1999–2049 (2020).
 36. Xie, P. & Arkin, P. A. Global Precipitation: A 17-Year Monthly Analysis Based on Gauge Observations, Satellite Estimates, and Numerical Model Outputs. *Bull. Am. Meteorol. Soc.* **78**, 2539–2558 (1997).
 37. Menemenlis, D. et al. ECCO2: High resolution global ocean and sea ice data synthesis. *Mercato. Ocean Q. Newsl.* **31**, 13–21 (2008).
 38. Su, W., Charlock, T. P. & Rose, F. G. Deriving surface ultraviolet radiation from CERES surface and atmospheric radiation budget: Methodology. *J. Geophys. Res. Atmos.* **110**, 2005JD005794 (2005).
 39. Hobday, A. J. et al. A hierarchical approach to defining marine heatwaves. *Prog. Oceanogr.* **141**, 227–238 (2016).
 40. Hobday, A. et al. Categorizing and Naming Marine Heatwaves. *Oceanography* **13**, 313–342 (2018).
 41. Kajtar, J. B., Holbrook, N. J. & Hernaman, V. A catalogue of marine heatwave metrics and trends for the Australian. *Reg. J. South. Hemisph. Earth Syst. Sci.* **71**, 284–302 (2021).
 42. Takaya, K. & Nakamura, H. A Formulation of a Phase-Independent Wave-Activity Flux for Stationary and Migratory Quasigeostrophic Eddies on a Zonally Varying Basic Flow. *J. Atmos. Sci.* **58**, 608–627 (2001).
 43. Holbrook, N. J. et al. A global assessment of marine heatwaves and their drivers. *Nat. Commun.* **10**, 2624 (2019).
 44. Mayer, J., Mayer, M. & Haimberger, L. Consistency and Homogeneity of Atmospheric Energy, Moisture, and Mass Budgets in ERA5. *J. Clim.* **34**, 3955–3974 (2021).
 45. Yanai, M., Esbensen, S. & Chu, J.-H. Determination of Bulk Properties of Tropical Cloud Clusters from Large-Scale Heat and Moisture Budgets. *J. Atmos. Sci.* **30**, 611–627 (1973).
 46. Neale, R. B. et al. Description of the NCAR Community Atmosphere Model (CAM 5.0). *NCAR TECHNICAL NOTE* (2012).
- (2019YFA0606701), the National Natural Science Foundation of China (42192564 & 42106202), the Strategic Priority Research Program of the Chinese Academy of Sciences (XDB42000000), and the development fund of South China Sea Institute of Oceanology of the Chinese Academy of Sciences (SCSIO202208). The numerical simulation is supported by the High Performance Computing Division in the South China Sea Institute of Oceanology. We appreciate the suggestions from Dr. Lei Zhang, Dr. Yuwei Hu and Dr. Ziqian Wang. We also thank Dr. Jules B. Kajtar for publicly releasing the codes of MHW metrics.

Author contributions

Q.S. designed the study, conducted the analysis and wrote the paper. C.W. and Y.Y. contributed to the study design, discussion of the results, the writing and revision of the manuscript. Q.S. and H.F. were involved in the design of CAM5 model experiments. All authors (Q.S., C.W., Y.Y., and H.F.) read and approved the final manuscript.

Competing interests

The authors declare no competing interests.

Additional information

Supplementary information The online version contains supplementary material available at <https://doi.org/10.1038/s41612-024-00645-x>.

Correspondence and requests for materials should be addressed to Chunzai Wang or Yulong Yao.

Reprints and permissions information is available at <http://www.nature.com/reprints>

Publisher's note Springer Nature remains neutral with regard to jurisdictional claims in published maps and institutional affiliations.

Open Access This article is licensed under a Creative Commons Attribution 4.0 International License, which permits use, sharing, adaptation, distribution and reproduction in any medium or format, as long as you give appropriate credit to the original author(s) and the source, provide a link to the Creative Commons licence, and indicate if changes were made. The images or other third party material in this article are included in the article's Creative Commons licence, unless indicated otherwise in a credit line to the material. If material is not included in the article's Creative Commons licence and your intended use is not permitted by statutory regulation or exceeds the permitted use, you will need to obtain permission directly from the copyright holder. To view a copy of this licence, visit <http://creativecommons.org/licenses/by/4.0/>.

© The Author(s) 2024

Acknowledgements

This research is supported by the National Natural Science Foundation of China (42192562), the National Key R&D Program of China